

Optimizing vortex pinning in $\text{YBa}_2\text{Cu}_3\text{O}_{7-x}$ superconducting films up to high magnetic fields

Ferran Vallès¹[✉], Anna Palau¹, Dmytro Abraimov², Jan Jaroszynski², Anca-Monia Constantinescu², Bernat Mundet¹, Xavier Obradors¹, David Larbalestier² & Teresa Puig¹[✉]

The magnetic flux pinning capabilities of $\text{YBa}_2\text{Cu}_3\text{O}_{7-x}$ (YBCO) coated conductors vary strongly across different regions of the magnetic field-temperature phase diagram and with the orientation of the magnetic field θ . Here, we determine the optimal pinning landscape for a given region of the phase diagram by investigating the critical current density $J_c(H, \theta, T)$ in the 5–77 K temperature range, from self-field to high magnetic fields of 35 T. Our systematic analysis reveals promising routes for artificially engineering YBCO coated conductors in any region of interest of the phase diagram. In solution-derived nanocomposites, we identify the relevance of coexisting high amounts of short stacking faults, Cu-O vacancy clusters, and segmentation of twin boundaries, in combination with nanoparticles, for enhanced pinning performance at high magnetic fields and low temperatures. Moreover, we demonstrate that twin boundaries preserve a high pinning energy in thick YBCO films, which is beneficial for the pinning performance at high magnetic fields and high temperatures.

¹Institut de Ciència de Materials de Barcelona (ICMAB-CSIC), Campus de la UAB, 08193 Bellaterra, Catalonia, Spain. ²Applied Superconductivity Center, National High Magnet Field Laboratory, Florida State University, Tallahassee, FL 32310, USA. ✉email: fvalles@icmab.es; teresa.puig@icmab.es

The successful development of suitable methods to grow epitaxial REBa₂Cu₃O_{7-x} (REBCO, RE = Rare Earth) films on top of bi-axially textured substrates following a multi-layered architecture (i.e., coated conductors), opened the way to promote practical and scalable conductors for power applications at high magnetic fields and temperatures¹⁻⁶. Among investigated superconductors, the REBCO superconductors do not exhibit either the highest critical temperature T_c or upper critical magnetic field H_{c2} . However, they do provide the highest irreversibility line H_{irr} (see Fig. S1 in the supplementary information for YBCO). Therefore, besides being suitable for power cables and fault current limiters at low magnetic fields and high temperatures⁷, REBCO coated conductors have been included in the design and fabrication of new coil architectures for high magnetic field applications such as research magnets⁸⁻¹², NMR/MRI magnets¹³, magnets for fusion energy¹⁴⁻¹⁶, and high energy physics accelerator magnets¹⁷. They are excellent candidates not only for superconducting large currents in high field magnets at very low temperatures, but also in the intermediate magnetic fields generated in rotating machines¹⁸ or superconducting magnetic energy storage systems^{19,20} at temperatures in the range of 20–50 K, which can be effectively driven by cryocoolers²¹.

At present, the magnetic field–temperature (H – T) ranges attainable with REBCO coated conductors are much wider than the ones obtained using any other existing superconducting material. However, the intrinsic limit of the dissipation-free current, i.e., the critical current density J_c , shows a strong variation in different regions of the H – T diagram and with the orientation of the magnetic field θ . Such variations are determined by the different vortex pinning contributions that arise in each microstructure and lead to different phases of the vortex lattice²²⁻²⁵. A quest for an adequate microstructure that favours vortex pinning and enhances J_c has been ongoing for the last decades, motivating the search for new nanoengineering approaches aimed at tuning the REBCO defect landscape with additional pinning centres^{4,5,26-32}.

Vortex pinning investigations based on the correlation between the electrical transport and microstructural visualization techniques enabled the evaluation of how each type of defect affects J_c enhancement. Nanoparticles^{16,27,33-36} improved the in-field J_c at all magnetic field orientations at any temperature and in some cases self-field (sf) J_c . The presence of random point defects^{37,38} also improved the in-field J_c , especially at temperatures below 40 K. Secondary phase nanorods/nanocolumns^{29,39,40} or irradiated columnar defects^{26,31} enhanced J_c mainly when H is parallel to the c -axis ($H||c$), especially at high magnetic fields and high temperatures; the same occurred for natural defects such as twin boundaries^{41,42} and dislocations^{43,44}. Lately, hybrid nanostructures combining various defects⁴⁵⁻⁵⁰ have also been investigated, with the aim of merging gains. However, only a few studies cover large magnetic field and temperature ranges^{6,51-53}.

In this article, we offer a broad study so as to determine the optimal microstructure for specific H – T conditions. We aim to identify relevant vortex pinning contributions in the widest possible range of the H – T diagram of YBCO, with special focus on very high magnetic fields. To do so, we analyse films that display a manifold microstructure, which we achieved with the versatile chemical solution deposition (CSD) technique used to grow nanostructured superconducting nanocomposites. Our analysis involves a thorough evaluation of $J_c(H, \theta, T)$ over a very broad range of temperatures (5–77 K) and applied magnetic fields (0–35 T), combined with detailed microstructural investigations by scanning transmission electron microscopy (STEM) and x-ray diffraction (XRD).

Results

The epitaxial solution-deposited YBCO films we study in this work are ranging in thickness from 100 nm to 1 μ m. These have been grown by CSD with various precursor solutions: pristine YBCO, YBCO with additives for spontaneous segregation of nanoparticles (ss-nanocomposites), and YBCO with preformed nanoparticles (pn-nanocomposites). We grew samples with distinctive amounts of nanoparticles (0–12% mol) and diverse processing conditions (i.e., film deposition, heating ramp), yielding to very different defect landscapes⁵⁴⁻⁵⁶; all films have an oxygen doping state close to optimal doping, deduced from the temperature evaluation of the normalized resistivity⁵⁷.

Here, we consider the identification of defect contributions according to angular pinning performance and the associated pinning strength, as described previously⁵⁸. As explained in detail in Supplementary Fig. S2, in CSD YBCO we find, typically, isotropic defects (0D and 3D) such as copper-oxygen vacancy clusters^{38,59}, small nanoparticles, or nanostrain generated in partial dislocations surrounding the stacking faults³⁵. On the other hand, we observe planar anisotropic defects such as stacking faults parallel to the a – b planes^{60,61} (also named YBa₂Cu₃O₈ intergrowths) or twin boundaries parallel to the c -axis^{61,62}.

Regarding the associated pinning strength, the ratio between the pinning energy $U_p = (\mu_0/2)H_c^2 v_p$ and the thermal energy $k_B T$, where μ_0 is the vacuum permeability, H_c is the thermodynamic critical field, $(\mu_0/2)H_c^2$ is the condensation energy, v_p is the volume of the pinned vortex core and k_B is the Boltzmann constant, determines the thermal activation processes occurring for each kind of defect²⁸. On one hand, point defects (i.e., oxygen and copper vacancies) have sizes below the order of magnitude of the superconducting coherence length ξ leading to a v_p further below ξ^3 . As a consequence, $U_p/k_B T \ll 1$ and they are considered weak pinning centres. On the other hand, nanoparticles (with a pinned vortex length L_p of $\sim 1-5\xi$), nanostrain ($L_p \sim 1-5\xi$), stacking faults ($L_p \sim 10-10^3\xi$) and twin boundaries ($L_p \sim 10-10^3\xi$) possess $U_p/k_B T \approx 1-10^3$, and for this reason are considered strong pinning centres. Additionally, strong anisotropic intrinsic pinning⁶³ ($L_p > 10^2\xi$), originated in the layered structure of the YBCO itself, coexists with stacking fault pinning for H parallel to the a – b planes ($H||ab$)^{64,65}.

We present our results in three subsections: in subsection “Pinning regimes up to 9 T in the H – T phase diagram”, we evaluate the pinning performance in the H – T region 0–9 T and 5–77 K for pristine YBCO and a large batch of YBCO nanocomposites listed in table S1, distinguishing different pinning regimes for $H||c$ and $H||ab$; in subsections “Density, strength and energy scale of vortex pinning centres up to 9 T” and “Density, strength and energy scale of vortex pinning centres up to 35 T” we evaluate for $H||c$ the density, strength and energy scale of the pinning centres up to 9 T and to 35 T, respectively, in a group of samples possessing very disparate microstructures.

Pinning regimes up to 9 T in the H – T phase diagram. We obtained accurate surfaces of $J_c(H, T)$ for the main orientations of the magnetic field $H||c$ and $H||ab$ for pristine and nanocomposite films, as shown in Fig. 1. This was achieved by measuring $J_c(H)$ curves at 5, 20, 50, 65 and 77 K, linearly interpolating, and subsequently fitting the curves as a function of temperature considering both the weak and strong pinning contributions of $J_c(T)$ (i.e., $J_c^{wk}(T)$ and $J_c^{str}(T)$, respectively). Whereas weak pinning centres yield a fast temperature decay of the J_c in the collective pinning model⁶⁶, strong pinning centres account for a smoother temperature decay in the Bose glass model²⁴. In a first approximation, we can describe $J_c(T)$ by the direct sum²⁸:

$$J_c(T) = J_c^{wk}(T) + J_c^{str}(T) = J_c(0)^{wk} \exp(-T/T_0) + J_c(0)^{str} \exp(-3(T/T^*)^2), \quad (1)$$

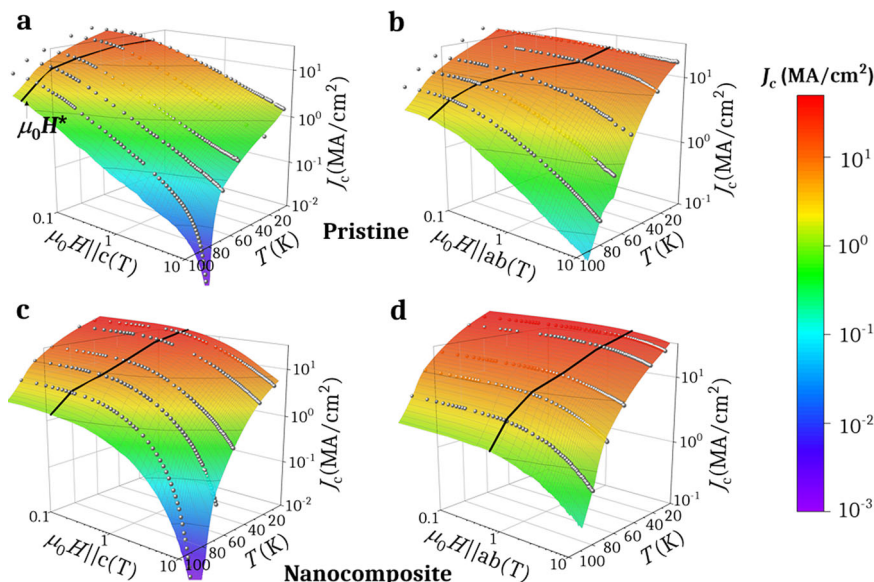


Fig. 1 $J_c(H, T)$ surfaces. $J_c(H, T)$ for (a, b) a pristine and (c, d) a nanocomposite for (a, c) $H \parallel c$ and (b, d) $H \parallel ab$. Spherical symbols represent the measured $J_c(H)$ curves and solid lines correspond to the accommodation magnetic field $\mu_0 H^*(T)$ curve.

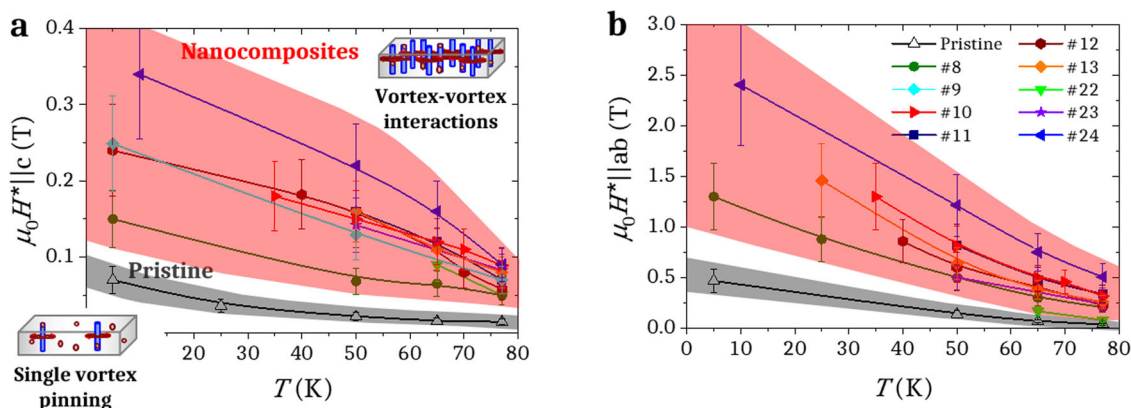


Fig. 2 Pinning regimes in the H - T diagram. Temperature dependence of $\mu_0 H^*$ for (a) $H \parallel c$ and (b) $H \parallel ab$ for pristine and ss-nanocomposites (sample details are indicated in supplementary table S1). $\mu_0 H^*(T)$ separates single vortex pinning from vortex-vortex interactions regimes in the H - T diagram. Error bars are determined by the standard deviation of $\mu_0 H^*$ for iterative measurements.

where $J_c(0)^{\text{wk}}$ and $J_c(0)^{\text{str}}$ refer to contributions at 0 K, whereas T_0 and T^* refer to temperatures associated to the characteristic vortex pinning energy of weak and strong defects, respectively. The final temperature interpolation is explained in detail in Supplementary Fig. S3.

It is worth stressing that the linear sum of contributions used in Eq. (1) and in Eq. (2) (in subsection “Density, strength and energy scale of vortex pinning centres up to 9 T”) is an approximation and does not take into account interaction between defects. The validity of the fitting parameters is strongly accurate when one pinning contribution dominates, otherwise the parameters are illustrative of tendencies. However, this model has demonstrated to be very successful in fitting the temperature dependence of J_c except in the high temperature and high magnetic field range ($T > 60$ K, $\mu_0 H > 2$ T) and correlates very well with the microstructural modifications of YBCO^{28,54,58,67–69}.

For the nanocomposite, the 3D $J_c(H, T)$ representation in Fig. 1 illustrates an enlargement of the (reddish) high critical current density region (>1 MA cm^{-2}) at low temperatures and low magnetic fields; the appealing region for high-current applications. On the other hand, at high temperatures and high magnetic

fields, a rapid decay of J_c is visible at lower H - T values for $H \parallel c$, but not for $H \parallel ab$.

The enlargement of the reddish high $J_c(H, T)$ region is concurrent with the shift to larger magnetic fields of the $\mu_0 H^*(T)$ curve, where H^* is the accommodation magnetic field, which sets the limit between the single vortex pinning regime—where vortices interact weakly with each other but strongly with defects^{70,71}—and the vortex-vortex interaction regime. Therefore, H^* is related to the density of defects. Here, it is defined as in other works^{58,72} by the equation $J_c(\mu_0 H^*) = 0.9J_c(\text{sf})$, where sf stands for self-field. Figure 2 shows a comparison between $\mu_0 H^*(T)$ curves for several nanocomposites and a pristine sample, for both $H \parallel c$ and $H \parallel ab$, highlighting the presence of the two regimes in the H - T diagram. In comparison to the pristine YBCO, all nanocomposites share the capability of enlarging the single vortex pinning regime up to high fields; this was observed for both magnetic field orientations, suggesting that the origin of this enlargement is effective at any orientation and, therefore, is isotropic.

In order to separate the isotropic (J_c^{iso}) and anisotropic (J_c^{aniso}) contributions of the $J_c(H)$ curves shown in Fig. 1 we applied the Blatter scaling approach^{28,73} to angular $J_c(\theta)$ measurements at

temperatures of 5, 20, 50, 65 and 77 K, and applied magnetic fields of 0.1, 0.3, 0.5, 1, 3, 5, 7 and 9 T. Subsequently, we fitted their temperature dependence through the procedure explained in the Supplementary information (fig. S3), aiming to establish the weight of each contribution within the full range of the H - T diagram.

We, thus, obtained the colour maps presented in Fig. 3, which show the ratio J_c^{iso}/J_c in the H - T diagram (equivalent to $1 - J_c^{\text{aniso}}/J_c$

by assuming a no interaction approximation), identifying regions of pinning dominance. For $H \parallel c$, we observe that the dominance of isotropic pinning is enhanced for the nanocomposite in both temperature and magnetic field, leaving the region dominated by anisotropic pinning close to the irreversibility line. For $H \parallel ab$, the dominance of isotropic pinning is also shifted to larger magnetic fields of the order of 1 T, especially at low temperatures.

It is worth noting that the $\mu_0 H^*(T)$ curves fall inside the region mostly dominated by isotropic pinning, in agreement with an increase of H^* related to the increase of isotropic pinning centres in nanocomposites. In contrast, we observe a slight decrease of $H_{\text{irr}}(T)$ for the nanocomposite, especially at $H \parallel c$, which can be associated to a lower pinning performance of the anisotropic defects (mainly twin boundaries⁴²).

To elucidate the origin of the variation between the isotropic and anisotropic pinning contributions, let us consider the correlation between the increase of H^* and the isotropic nanostrain; the nanostrain arises in the region surrounding the partial dislocations that envelope the stacking faults (Supplementary Fig. S2c, d), and it has been signalled as a characteristic defect emerging in large quantities in nanocomposites³⁵. Hence, we macroscopically measured the nanostrain (ϵ) for each sample by XRD analysis, following the Williamson-Hall method⁷⁴.

Figure 4a-f shows the above-mentioned correlation between the H^* accommodation magnetic field (measured at 5, 50 and 77 K for both $H \parallel c$ and $H \parallel ab$) and nanostrain for a very broad variety of samples (listed in the supplementary table S1). Although the results do not fall exactly on a single curve, we observe a common trend of the exponential increase of H^* when ϵ increases; this is clear at all temperatures and orientations of the

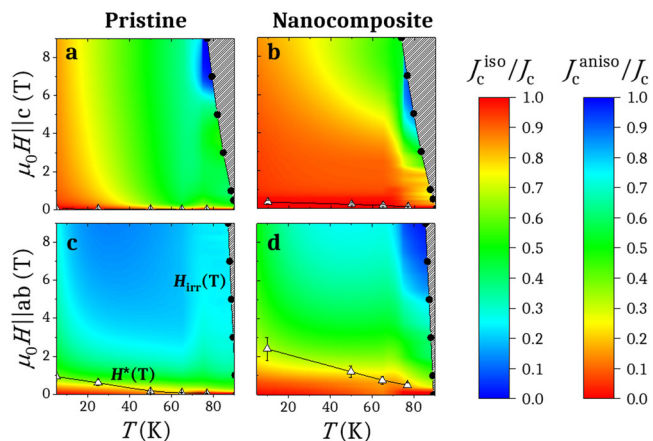


Fig. 3 J_c^{iso}/J_c and J_c^{aniso}/J_c in the H - T diagram. $\mu_0 H$ - T colour map of the ratios J_c^{iso}/J_c and J_c^{aniso}/J_c for (a, c) a pristine and (b, d) a nanocomposite for (a, b) $H \parallel c$ and (c, d) $H \parallel ab$. Solid lines with circles and triangles mark the $\mu_0 H_{\text{irr}}(T)$ and $\mu_0 H^*(T)$ curves, respectively. Error bars are determined by the standard deviation of $\mu_0 H^*$ for iterative measurements.

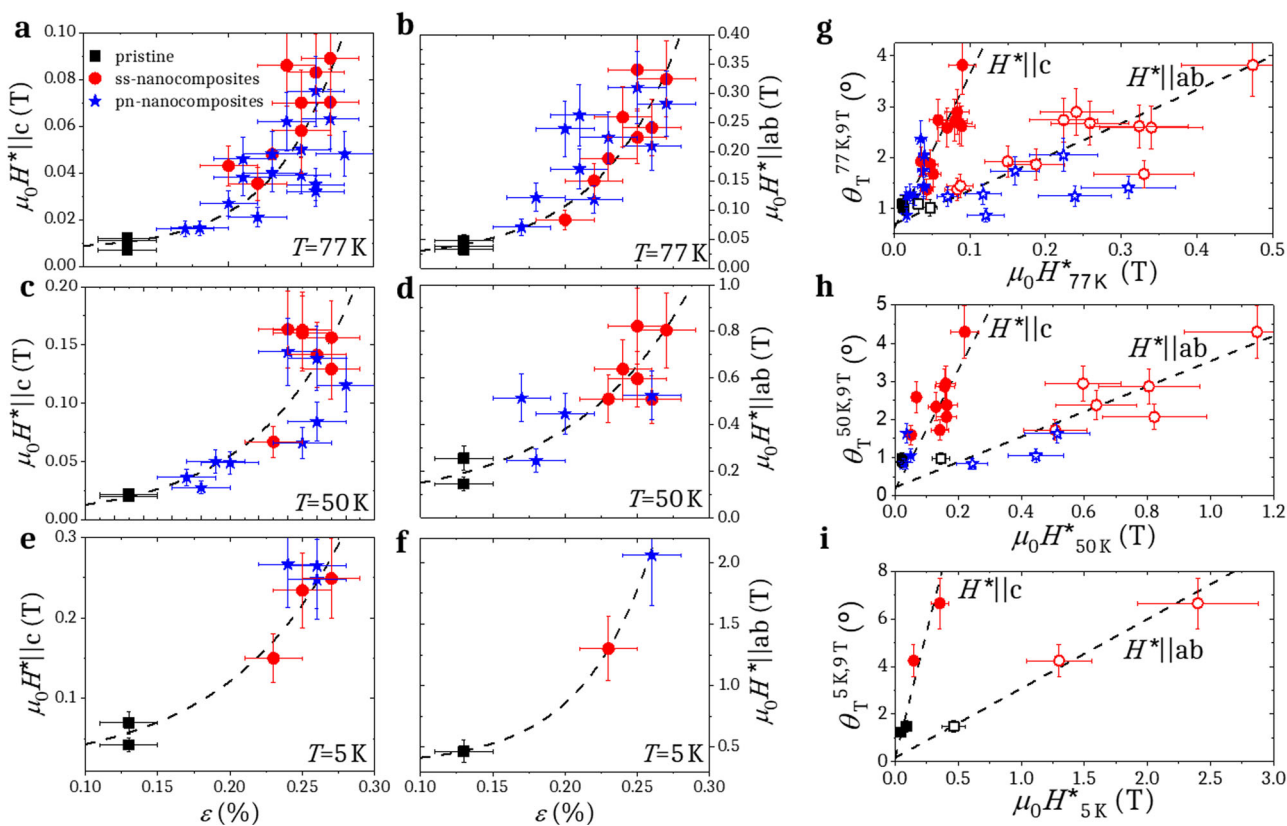


Fig. 4 Exponential $H^*(\epsilon)$ and linear $\theta_T(H^*)$ trends. For (black) pristine, (red) ss-nanocomposites and (blue) pn-nanocomposites: $\mu_0 H^*$ at (a, b) 77 K, (c, d) 50 K and (e, f) 5 K for (a, c, e) $H^* \parallel c$ and (b, d, f) $H^* \parallel ab$ versus nanostrain and θ_T at 9 T as a function of $\mu_0 H^*$ at (g) 77 K, (h) 50 K and (i) 5 K for $H^* \parallel c$ (closed symbols) and $H^* \parallel ab$ (open symbols). Dashed lines are guides to the eye. Error bars are determined by the standard deviation of iterative measurements for $\mu_0 H^*$ and θ_T and by the standard error of the fitting of the Williamson-Hall method⁷⁴ in the case of ϵ .

Table 1 Sample properties.

Name	Composition	<i>t</i> (nm)	<i>T_c</i> (K)	ΔT_c (K)	$J_c^{st,77\text{ K}}$ (MA cm ⁻²)	$\mu_0 H_{irr}^{H c,77\text{ K}}$ (T)	ϵ (%)	$\langle \varnothing_{NP} \rangle$ (nm)	σ_{NP} (nm ⁻²)	$\langle d_{SF} \rangle$ (nm)	λ_{SF} (nm ⁻¹)
pr-thin-1	Pristine YBCO	250	90.0	1.4	4.2	9.4	0.13	—	none	140	low
pr-thin-2	Pristine YBCO	250	92.7	3.1	4.3	n.m.	0.13	—	none	140	low
pr-thick	Pristine YBCO	600	91.4	2.4	2.0	9.0	n.m.	58	low	150	low
ss-nc-thin-1	YBCO+8%BYTO	250	90.2	1.0	3.5	7.7	0.20	13	medium	140	high
ss-nc-thin-2	YBCO+10%BZO&5%YO	250	91.7	1.8	3.0	7	n.m.	17	medium	45	high
pn-nc-thin	YBCO+20%BHO	150	88.6	5.7	3.0	5.4	0.24	8	high	8	medium
pn-nc-thick	YBCO+20%BZO	700	92.5	2.7	3.4	9.3	0.26	19	high	95	medium

t thickness, *T_c* critical temperature, ΔT_c transition width, $J_c^{st,77\text{ K}}$ critical current density at 77 K and self-field, $H_{irr}^{H||c,77\text{ K}}$ irreversibility magnetic field at 77 K for $H||c$, ϵ nanostrain, $\langle \varnothing_{NP} \rangle$ average nanoparticle diameter, σ_{NP} density of nanoparticles, $\langle d_{SF} \rangle$ average stacking fault length and λ_{SF} density of stacking faults. pr: pristine, nc: nanocomposite, ss: spontaneously segregated nanoparticles, pn: preformed nanoparticles, n.m.: not measured. σ_{NP} ranges: low ($\sigma_{NP} < 1E-4\text{ nm}^{-2}$), medium ($1E-4\text{ nm}^{-2} < \sigma_{NP} < 5E-4\text{ nm}^{-2}$), high ($\sigma_{NP} > 5E-4\text{ nm}^{-2}$). λ_{SF} ranges: low ($\lambda_{SF} < 0.1\text{ nm}^{-1}$), medium ($0.1\text{ nm}^{-1} < \lambda_{SF} < 0.15\text{ nm}^{-1}$), high ($\lambda_{SF} > 0.15\text{ nm}^{-1}$). YBCO, BHO, BZO, BYTO and YO stand for $YBa_2Cu_3O_{7-x}$, $BaHfO_3$, $BaZrO_3$, Ba_2YTaO_6 and Y_2O_3 respectively.

magnetic field considered. This correlation explains the importance of the isotropic nanostrain but, based on the deviations from the trend, it also reveals that this cannot be strictly distinguished as the unique cause of the enlargement of H^* . Small nanoparticles able to pin vortices by themselves might well be an additional contribution of this enlargement.

Further, we analysed the widening of the $J_c^{aniso}(\theta)$ ab-peak; we approximated its half width-half-maximum with the trapping angle θ_T that limits the vortex staircase regime^{64,75} (θ_T calculation presented in Supplementary Fig. S4), which in this case can be interpreted as an additional capability of accommodating vortices parallel to the ab-planes due to a higher presence of stacking faults. Figure 4g-i presents θ_T versus $\mu_0 H^*$ at temperatures of 77, 50 and 5 K for $J_c(\theta)$ curves measured at a field of 9 T and for $J_c(H)$ curves measured for both $H||c$ and $H||ab$. The linear trend of the $\theta_T(H^*)$ combined with the exponential trend of $H^*(\epsilon)$ indicates that the introduction of stacking faults leads to a vortex trapping widening and an increase of isotropic pinning centres by means of nanostrain. Some deviations from the $\theta_T(H^*)$ trend are observed when $H^*||ab$, which can be associated with H^* enhancement provided by stacking faults themselves, additional to the pinning of small nanoparticles already commented in the previous paragraph.

Density, strength and energy scale of vortex pinning centres up to 9 T. To separate the characteristics of different vortex pinning centres, we combined $J_c(T)$ curves obtained for a wide range of magnetic fields with $J_c(\theta)$ curves obtained at specific temperatures, and applied the Blatter scaling approach^{28,73}. Thus, we determined the $J_c^{iso}(T)$ and $J_c^{aniso}(T)$ components.

We determined curves up to 35 T for a broad variety of samples that are representative of different microstructures, consisting of pristine and nanocomposite films with Ba_2YTaO_6 (BYTO), $BaZrO_3$ (BZO), Y_2O_3 (YO), or $BaHfO_3$ (BHO) nanoparticles (note that in this subsection we present only the results obtained up to 9 T; the results up to 35 T are summarized in the next subsection).

In Table 1 are shown the thickness (*t*), nanostrain (ϵ), nanoparticle (NP) average diameter ($\langle \varnothing_{NP} \rangle$) and density (σ_{NP}), stacking fault (SF) average length ($\langle d_{SF} \rangle$) and density (λ_{SF}) and main electrical transport properties—*T_c*, ΔT_c (transition width), $J_c^{st,77\text{ K}}$ and $H_{irr}^{H||c,77\text{ K}}$ —of each of the samples we analysed. All samples display $T_c > 88\text{ K}$, $\Delta T_c < 6\text{ K}$, and $J_c^{st,77\text{ K}} \approx 2\text{--}4.5\text{ MA cm}^{-2}$. We evaluated $H_{irr}^{H||c,77\text{ K}}$ from $J_c(H)$ measurements fulfilling the relation $J_c(H_{irr}) = 10^{-4} J_c(sf)$.

We inferred the NP and SF average densities from the high-angle annular dark field (HAADF) STEM images shown in Supplementary Fig. S5 using the formulae $\sigma_{NP} = n_{NP}/A_{YBCO}$ and $\lambda_{SF} = \sum d_{SF}/A_{YBCO}$, where n_{NP} is the number of nanoparticles and A_{YBCO} is the area of the image corresponding to the analysed YBCO film. The identification of nanoparticles, stacking faults

and the area A_{YBCO} needed for these calculations are illustrated in Supplementary Fig. S6.

From Table 1, one observes that pristine films display a larger irreversibility magnetic field than nanocomposite films (except for pn-nc-thick); this indicates a significant change of the dominating pinning defect at high magnetic fields. Further, all nanocomposites exhibit a medium or high density of nanoparticles and stacking faults. However, each sample displays significant changes of the distribution and sizes of these defects. The ss-nc-thin-2 and pn-nc-thin films show significantly shorter stacking faults than the rest of the films; this indicates a larger presence of partial dislocations. Furthermore, the pn-nc-thin film is characterized by very small nanoparticles with diameters very close to ξ (2 or 3 times) at the measured temperature.

Anisotropic defects act only as strong pinning centres, whereas isotropic defects can be either point or nanosized defects, promoting both weak and strong pinning. Therefore, the total $J_c(T)$ can be described by the linear sum of three contributions:

$$J_c(T) = J_c^{iso-wk}(T) + J_c^{iso-wk}(T) + J_c^{aniso-str}(T) \\ = J_c(0)^{iso-wk} \exp(-T/T_0) + J_c(0)^{iso-str} \exp(-3(T/T_{iso-str}^*)^2) \\ + J_c(0)^{aniso-str} \exp(-3(T/T_{aniso-str}^*)^2), \quad (2)$$

where the J_c^{str} contribution from Eq. (1) is substituted now by the sum of the isotropic-strong (iso-str) contribution $J_c^{iso-str}$ and the anisotropic-strong (aniso-str) contribution $J_c^{aniso-str}$ (corresponding directly to J_c^{aniso}); the isotropic-weak (iso-wk) contribution J_c^{iso-wk} corresponds to the overall J_c^{wk} contribution.

For the films that were studied in this work, we considered that iso-wk is generally associated to atom/cluster vacancies, iso-str to nanostrained regions and nanoparticles, and aniso-str to twin boundaries for $H||c$. Regarding the nanoparticles, they become effective pinning centres when their diameter is sufficiently small (below 8 nm)^{36,56,76}. By fitting Eq. (2) to the experimental results obtained at different magnetic fields, we determined the field dependence of the fitting parameters; these are the characteristic temperatures T_0 , $T_{iso-str}^*$, and $T_{aniso-str}^*$ and the contributions at 0 K $J_c(0)^{iso-wk}$, $J_c(0)^{iso-str}$, and $J_c(0)^{aniso-str}$. T_0 , $T_{iso-str}^*$ and $T_{aniso-str}^*$ are associated with the characteristic pinning energy of the defects, they account for the effectiveness of their pinning potential in relation with the thermal energy $k_B T$. Instead, $J_c(0)^{iso-wk}$, $J_c(0)^{iso-str}$, and $J_c(0)^{aniso-str}$ are the J_c values at 0 K of each pinning contribution in the absence of creep; thus, they are proportional to the density and strength of pinning centres. On the other hand, the accommodation magnetic field $\mu_0 H^*(0\text{ K})$ obtained in $J_c(0)$ vs. magnetic field curves is exclusively associated to the density of pinning centres.

In Fig. 5a are shown the characteristic temperatures vs. the applied magnetic field. Coloured bands highlight the dispersion range of the characteristic temperatures obtained for different samples (i.e., $T_0 = 5\text{--}20\text{ K}$, $T_{iso-str}^* = 50\text{--}90\text{ K}$ and $T_{aniso-str}^* = 70\text{--}130\text{ K}$).

We note that the characteristic temperatures for each contribution are characterized by similar ranges regardless of

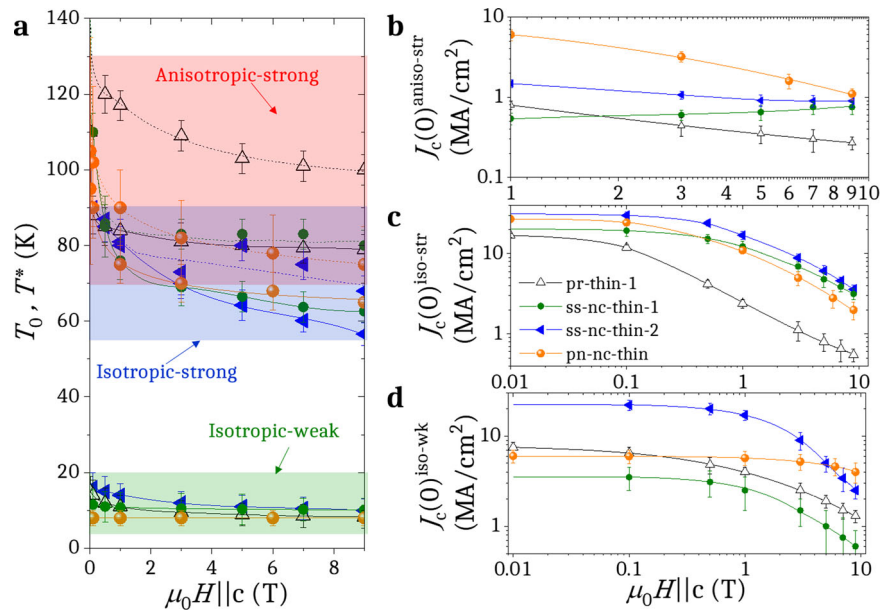


Fig. 5 Characteristic temperatures, density and strength of pinning centres for $H || c$. Applied magnetic field dependence of characteristic temperatures (a) T_0 (solid lines, green region), $T_{iso-str}^*$ (solid lines, blue region) and $T_{aniso-str}^*$ (dashed lines, red region), and J_c contributions at 0 K (b) $J_c(0)^{aniso-str}$, (c) $J_c(0)^{iso-str}$ and (d) $J_c(0)^{iso-wk}$ for pr-thin-1, ss-nc-thin-1, ss-nc-thin-2 and pn-nc-thin samples for $H || c$. Error bars are determined by the standard error of the parameters from the fitting of Eq. (2).

the sample type, indicating that the same type of defects contribute in different samples. However, differences in size and/or precise morphology of the defects induce significant changes. The larger dispersion in the pinning energy values was obtained for $T_{aniso-str}^*$. In this case, much lower values are found for all nanocomposites ($T_{aniso-str}^* \approx 70\text{--}80$ K at high fields) as compared with the pristine, which we associate to the segmentation of twin boundaries due to a large density of stacking faults^{42,62} (Supplementary Fig. S2e, f). This segmentation provokes a decrease of L_p which yields to less anisotropic pinning at high temperatures and a reduction of the irreversibility line H_{irr} ²⁴. In contrast, the pristine sample shows the highest $T_{aniso-str}^*$ values and largest H_{irr} (9.4 T at 77 K, Table 1), indicative of coherent long twin boundaries²⁴. Another remarkable difference is the one obtained for $T_{iso-str}^*$, which also shows lower values for nanocomposites than for the pristine, suggesting a change in the nature of isotropic-strong pinning centres, in agreement with the introduction of nanoparticles and the abundant pinning provided by nanostrain in nanocomposites.

Regarding the 0 K contributions of J_c , we also observe remarkable differences between nanocomposites and the pristine sample. In the case of iso-wk (Fig. 5d), we observe that nanocomposites show an enhanced $\mu_0 H_{iso-wk}^*(0\text{ K})$, specially the pn-nc-thin, which is ascribed to a high density of Cu-O vacancy clusters hosted in the stacking faults^{38,59}. The best $J_c(0)^{iso-wk}$ contribution is found for ss-nc-thin-2, in agreement with a large number of Cu-O vacancies which are stronger in this sample (see T_0 in Fig. 5a). In the case of iso-str pinning in Fig. 5c, nanocomposites exhibit altogether a distinguishable behaviour with respect to the pristine film due to the nanostrain already mentioned in the previous subsection, resulting in enhanced $J_c(0)^{iso-str}$ at any magnetic field. In addition, nanoparticles that are sufficiently small will also contribute to enhance iso-str pinning. Last, the aniso-str pinning in Fig. 5b, mainly attributed to the pinning performance of twin boundaries, shows that pn-nc-thin and ss-nc-thin-2 films excel at exhibiting the largest $J_c^{aniso-str}$ values along the entire studied range, which is certainly related to a very high density of twin boundaries due to their segmentation and therefore multiplication provoked by the presence of a high density of short

stacking faults as observed in these films (Supplementary Fig. S5d, e, g, h). Therefore, this evidences that a high density of short stacking faults coexists with a high density of twin boundaries, which however, produce a lower $T_{aniso-str}^*$ due to the lack of vertical defect coherence.

Density, strength and energy scale of vortex pinning centres up to 35 T. Nanocomposites improve J_c primarily in magnetic field regions where the isotropic pinning contribution is enhanced. However, studies up to very high magnetic fields highlight that a crossover may occur, resulting in lower J_c of nanocomposites in comparison to pristine films, especially at high temperatures due to the high $T_{aniso-str}^*$ values developed by pristine films. The $J_c(H, T)$ surfaces of pr-thin-2 and pn-nc-thin are compared in Fig. 6a, b at 5–60 K and 10–35 T. It is recognized that the pn-nanocomposite displays larger critical current densities in a large H - T region, especially at low temperatures and intermediate fields. In contrast, at high temperatures and large magnetic fields, the nanocomposite presents a more prominent decay of J_c associated with its lower irreversibility field.

We observe in Fig. 6c that although the pn-nc-thin sample exhibits a fast $J_c(H)$ decay at 30 K with lower J_c values at very high fields, it shows the best performance at 4.2 K at the entire analysed magnetic field range. A crossover between the J_c values from pn-nc-thin and pr-thin-2 is expected to take place at a magnetic field higher than 35 T. Such a crossover is on the other hand observed at 25 T between pn-nc-thin and pr-thin-2.

At 30 K, a desirable temperature for superconducting rotating machinery applications¹⁸ refrigerated with cryocooler technology²¹, nanocomposites also offer substantially larger J_c values than pristine films in the magnetic field region of 5–20 T, strengthening the fact that nanocomposites are very appropriate for the development of coated conductors for in-field applications. On the other hand, as depicted in Fig. 6d, thick films offer at 4.2 K higher total critical current J_c values in comparison with the pristine thin film up to 35 T, despite of their lower J_c values. This reinforces the need to further understand and optimize the growth of thick films (using inkjet

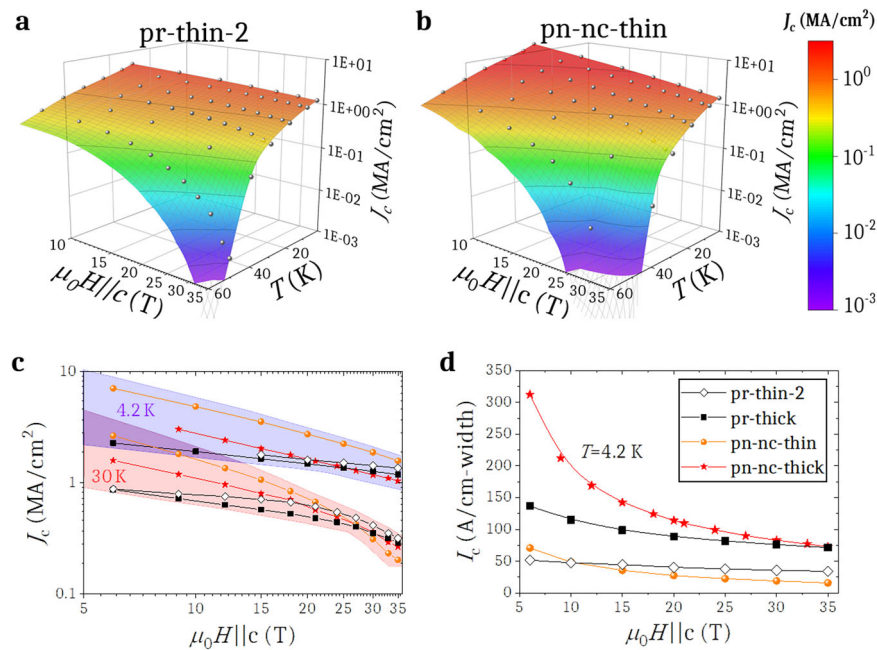


Fig. 6 $J_c(H,T)$ surfaces, $J_c(H)$ and $I_c(H)$ at very high magnetic fields for $H \parallel c$. $J_c(H,T)$ surfaces for (a) pr-thin-2 and (b) pn-nc-thin. Magnetic field dependence of (c) J_c at 4.2 K (blue region) and 30 K (red region) and of (d) I_c at 4.2 K for pr-thin-2, pr-thick, pn-nc-thin and pn-nc-thick samples.

printing in this case⁷⁷). Our study on CSD films suggests that the selection of thick nanocomposite films is especially beneficial for the design of coated conductors operating at the range of 5–10 T offering 6 and 2.5 times larger I_c values than the thin and thick pristine films respectively.

Additionally, in the high magnetic field facilities, we have been able to analyse the isothermal magnetic field dependent current-voltage characteristics for four different samples: pr-thin-2, pr-thick, pn-nc-thin and pn-nc-thick, whose pinning force density $F_p(H)$ curves are plotted in Supplementary Fig. S7. In these plots, we focus at three H – T conditions: [50 K,15 T], [50 K,35 T] and [4.2 K,35 T], summarized in Table 2. Notice that different samples provide the best F_p -value at each condition: the thick pn-nanocomposite provides 45 GN m⁻³ at [50 K,15 T], the pristine thick film 4 GN m⁻³ at [50 K,35 T] and the thin pn-nanocomposite 0.55 TN m⁻³ at [4.2 K,35 T]. In order to understand the responsible pinning contributions at the different H – T conditions, we have extended the study from the previous subsection to magnetic fields up to 35 T, obtaining the magnetic field dependence of the characteristic temperatures T_0 , $T_{\text{iso-str}}^*$ and $T_{\text{aniso-str}}^*$ and the J_c contributions at 0 K, $J_c(0)_{\text{iso-wk}}$, $J_c(0)_{\text{iso-str}}$ and $J_c(0)_{\text{aniso-str}}$, in Fig. 7. Interestingly, Fig. 7a shows that T_0 tends to slightly increase, whereas both $T_{\text{iso-str}}^*$ and $T_{\text{aniso-str}}^*$ tend to decrease with increasing magnetic field. The increase of T_0 can be related to a shrinking of the vortex core size with increasing magnetic field^{78,79} and the outbreak of other sources of weak pinning promoted by atomic defects of the order of Å. The performance at 30–50 K at very high magnetic fields is therefore very much influenced by the pinning characteristic temperatures.

The analysis of the pinning contributions extrapolated to 0 K shows in general larger $J_c(0)$ for pn-nanocomposites than for pristine samples (Fig. 7b–d), which makes nanocomposites very appealing for the application of superconducting films at helium temperature. The pn-nc-thin sample exhibits the largest values of iso-weak pinning due to the already mentioned Cu–O vacancies, and very large iso-str pinning up to 25 T due to the large density of nanostrained regions surrounding the short stacking faults and very likely due to the small BHO nanoparticles, and also a large aniso-str pinning due to the high density of segmented twin

Table 2 Pinning force densities for $H \parallel c$ at the temperature and magnetic field conditions: [50 K,15 T], [50 K,35 T] and [4.2 K,35 T].

Sample	F_p @ 50 K, 15 T (GN m ⁻³)	F_p @ 50 K, 35 T (GN m ⁻³)	F_p @ 4.2 K, 35 T (TN m ⁻³)
pr-thin-2	30	0.9	0.48
pr-thick	27	4	0.42
pn-nc-thin	29	<0.2	0.55
pn-nc-thick	45	3	0.36

F_p is pinning force density

boundaries. Altogether, it makes pn-nc-thin the best sample to afford a pinning force density of 0.55 TN m⁻³ at [4.2 K,35 T]. However, the low $T_{\text{iso-str}}^*$ and especially the low $T_{\text{aniso-str}}^*$ possessed by this thin pn-nanocomposite plotted in Fig. 7a cause a strong $J_c(H)$ decay at higher temperatures, as already observed in Fig. 6.

On the other hand, the thick pn-nanocomposite exhibits higher $T_{\text{iso-str}}^*$ and $T_{\text{aniso-str}}^*$ (Fig. 7a) than the thin pn-nanocomposite and ss-nanocomposites (Fig. 5a). Actually, this $T_{\text{iso-str}}^*$ coincides with that for pristine samples (note that the different thin pristine samples display in general very similar results), indicating that nanoparticles and nanostrained regions have not effectively modified the typology of pinning centres in the thick pn-nanocomposite, also manifested by the similar $J_c(0)_{\text{iso-str}}(H)$ dependence in Fig. 7c. $T_{\text{aniso-str}}^*$ in this sample is also closer to the one of pristine samples, indicating a regain in vertical coherence length of twin boundaries in comparison to thin nanocomposites. If we also consider the high $T_{\text{aniso-str}}^*$ obtained by the thick pristine, which is the highest at 35 T, all the signs are that larger thickness favours twin boundary coherence (and therefore longer L_p) and yields to a higher value of $T_{\text{aniso-str}}^*$. The longer twin boundary coherence can be given by any of two reasons: i) large thickness promotes more regions in the microstructure which are less faulted (regions away from the surface and from the substrate interface) so that twin boundaries are less broken, ii) with large thickness it is

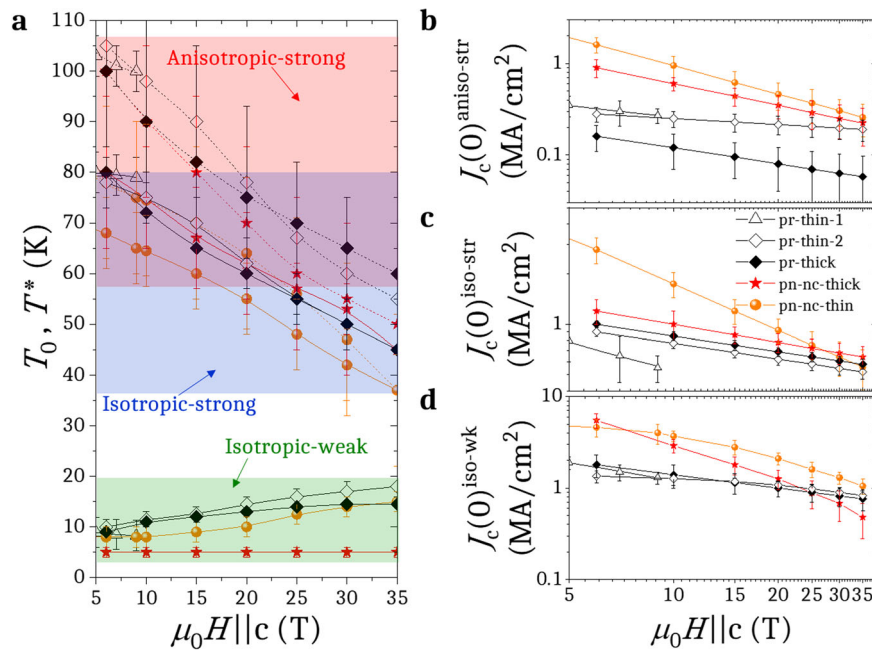


Fig. 7 Characteristic temperatures, density and strength of pinning centres at very high magnetic fields. Magnetic field dependence of characteristic temperatures (a) T_0 (solid lines), $T_{iso-str}^*$ (solid lines) and $T_{aniso-str}^*$ (dashed lines), and J_c contributions at 0 K (b) $J_c^{aniso-str}$, (c) $J_c^{iso-str}$ and (d) J_c^{iso-wk} for pr-thin-1, pr-thin-2, pr-thick, pn-nc-thin and pn-nc-thick samples for $H || c$ at very high magnetic fields. Error bars are determined by the standard error of the parameters from the fitting of Eq. (2).

easier to sum twin boundary segments which coincide vertically and contribute to a final longer L_p . For this enhanced $T_{aniso-str}^*$, pr-thick and pn-nc-thick exhibit the best pinning force densities at [50 K, 35 T] and [50 K, 15 T] respectively. Moreover, given the larger I_c in thicker films (Fig. 6d), the total pinning force strongly improves and therefore it is strongly recommended to take steps forward in the direction of gaining thickness.

The study of current–voltage curves at very high magnetic fields has been extended at magnetic orientations different to $H || c$ at the temperature of 20 K, covering an angular range of 180° centred at $H || ab$ for the magnetic fields of 15, 25 and 35 T. Results are plotted in Supplementary Fig. S8a for pr-thin-2, pn-nc-thin and pn-nc-thick. It is observed that the ab-peak is widened for nanocomposites, in agreement with a larger θ_T to accommodate vortices by stacking faults. Below the crossover magnetic field of about 20 T, where J_c values of nanocomposites fall below the ones of pristine films (in Fig. 6c at 30 K), nanocomposites offer higher performance throughout the angular range. In contrast, above 20 T, the pristine film starts to exhibit larger J_c than nanocomposites in the vicinity of $H || c$, where an intricate competition takes place between the three contributions (iso-wk, iso-str and aniso-str) since T_0 , $T_{iso-str}^*$ and $T_{aniso-str}^*$ get closer at very high magnetic fields (Fig. 7a). Notice that collapses of J_c^{iso} (Supplementary Fig. S8b) are obtained for effective anisotropies (γ_{eff}) of 6, 2.5 and 2 for pr-thin-2, pn-nc-thin and pn-nc-thick respectively, which are the same values that were obtained at lower magnetic fields. Thus, confirming that γ_{eff} remains constant at very high magnetic fields and that the effective anisotropy of the nanocomposite films is certainly approaching very low values, making them very appealing for high field magnets where the isotropic characteristics of CC are a strong demand.

Discussion

The thorough study undertaken at wide temperature and magnetic field ranges up to 35 T has demonstrated that the performance of solution-derived nanocomposites is excellent at very high magnetic fields and very low temperatures. However, at

temperatures above 20 K, there is a crossover of J_c values in nanocomposites with respect to the pristine films. This suggests that additional pinning centres should be induced at these conditions to overcome the existing performances of pristine CSD films, as for example promoting longer defect coherence or by a reinforcement of the density of small nanoparticles which can act as pinning centres themselves. The pinning characteristics observed in CSD films are specially ascribed to the shape, density and length of the most extended defect in these films, i.e. the stacking fault. In particular, from the analysis elaborated here we conclude that stacking faults in solution-derived YBCO nanocomposites have a triple effect in the pinning contributions for $H || c$:

They increase the isotropic-strong contribution by means of increasing $J_c(0)^{iso-str}$ due to the generation of isotropic nanosized strain regions located at the partial dislocations surrounding the stacking faults. This increase is very effective at low-intermediate magnetic fields and intermediate temperatures and is responsible for the general enlargement of the single vortex pinning regime defined by the increase of $\mu_0 H^*$. They increase the isotropic-weak contribution by means of increasing $J_c(0)^{iso-wk}$ due to the formation of Cu-O vacancy clusters among stacking faults. This increase is very effective at low temperatures.

They increase the anisotropic-strong contribution by means of increasing $J_c(0)^{aniso-str}$ due to the multiplication of twin boundaries given by the segmentation provoked by the appearance of stacking faults. The increase of $J_c(0)^{aniso-str}$ is very effective at low temperatures up to very high magnetic fields. However, the segmentation of twin boundaries causes in parallel a breaking of their vertical coherence, which yields a reduction of the pinning energy $T_{aniso-str}^*$ and therefore a decrease of the irreversibility line $\mu_0 H_{irr}(T)$, which can be recovered in the case of thick nanocomposites.

Therefore, the intensity of each change in any of the pinning contributions will strongly depend on the precise distribution and

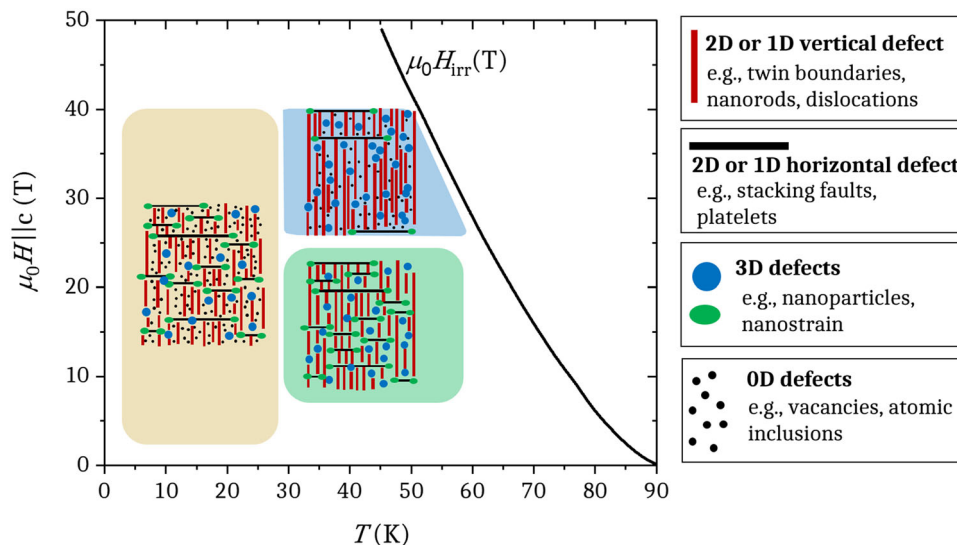


Fig. 8 Optimized pinning landscapes for $H \parallel c$. H - T diagram with three optimized pinning landscapes in the regions of: low temperatures from low magnetic fields to ~ 35 T, intermediate temperatures and intermediate magnetic fields (~ 15 T) and intermediate temperatures and very high magnetic fields (~ 35 T).

size of the stacking faults present in each sample. To summarize, we propose general optimized defect landscapes to enhance pinning at distinctive H - T regions for $H \parallel c$, depicted in Fig. 8:

At low T and from low to very high H : a large density of isotropic defects (e.g., Cu-O vacancies, nanostrain and small nanoparticles) and anisotropic defects (e.g., segmented twin boundaries), no matter their length in defect coherence. Therefore, a landscape possessing large density of short stacking faults and small nanoparticles is very appropriate.

At intermediate T and intermediate H : a large density of strong isotropic and anisotropic defects, the latter with a long vertical coherence (e.g., nanoparticles, nanostrain and twin boundaries or a mixed landscape of long nanorods combined with nanoparticles and nanostrain).

At intermediate T and high H : a high density of anisotropic-strong defects with a very long vertical coherence (like long twin boundaries in thick nanocomposites or elongated nanorods), if possible combined with other auxiliary strong or weak isotropic defects in order to sum pinning gains and avoid vortex creep excitations in parallel correlated defects^{36,45,80}.

Conclusions

Overall, the analysis presented here demonstrates the capacity to artificially modify the pinning landscape with solution-derived nanocomposites due to the benefits of adding small nanoparticles and the relevance of stacking faults and their secondary effects (generation of strained nanoregions, generation of Cu-O vacancy clusters and segmentation of twin boundaries). Furthermore, this study urges the manufacturers to fabricate customized coated conductors for different applications depending on their magnetic field and temperature operation range. Whereas the generation of a mixed landscape with plentiful kinds of defects of short length is desirable for enhancing pinning at low temperatures, the presence of strong elongated defects with long defect coherence in combination with other auxiliary defects is preferable for pinning at higher temperatures, and defects with even longer defect coherence in the case of very high magnetic fields.

Methods

YBCO film growth. Epitaxial c -axis oriented YBCO films were grown by chemical solution deposition from metal organic decomposition of trifluoroacetate salts in

solution following previous works^{81–83}. The solution was deposited on 5×5 mm LaAlO₃ single crystal substrates whether by spin coating for thin films (150–250 nm) or by inkjet printing for thick films (>600 nm)^{84,85}. Subsequently, films were pyrolyzed and thermal treated at high temperatures. All films in Table 1 have been grown following a conventional thermal annealing (25 °C min^{-1} heating ramp)⁸³, except the pn-nc-thin sample, which followed a flash heating process (1200 °C min^{-1} heating ramp)⁸⁶. Nanocomposites were obtained by promoting the formation of nanoparticles in the YBCO matrix, whether by including the salts directly to the solution leading to spontaneous segregation during growth (ss-nanocomposites)^{28,35} or by the mixing of a previously stabilized colloidal solution containing preformed nanoparticles with the trifluoroacetate precursor solution (pn-nanocomposites)^{55,56,87,88}. Nanoparticle concentrations are expressed by the percentage of the molar concentration of nanoparticles with respect to the YBCO molar concentration. For example, for YBCO + 8%BYTO there are 8 mols of BYTO for 100 mols of YBCO.

Electric transport measurements. Current-voltage curves were obtained using the standard four-point method. Silver contacts were sputtered on YBCO with a TSST sputtering system and were post-annealed, ensuring contact resistivities below 10 $\mu\Omega\text{-cm}^2$. Samples were trimmed into 10 – 100 μm narrow bridges with lengths of 200 – 400 μm by standard lithography with a Micro-Writer from Durham Magneto Optics LTD and wet etching in H_3PO_4 . The current was applied parallel to the a - b plane, always perpendicularly to the magnetic field which was rotated with the angle θ from the c -axis (0°) to the ab -plane (90°), ensuring maximum Lorentz force configuration. Critical currents were determined for a 10 $\mu\text{V cm}^{-1}$ electric field. The current-voltage characteristics up to 9 T were conducted in a Quantum Design PPMS 9 T system, whereas the experiments carried out up to 35 T were conducted in a cryostat inside of a 35 T DC resistive magnet (32 mm bore) using a tight-vacuum probe provided with a rotating sample holder (Fig. S9 in the supplementary information) and a temperature control system operating in the 4.2 – 60 K range.

Microstructural characterisation. Nanostrain (ϵ) was quantified along the c -axis by analysing the symmetric (001) 2θ Bragg XRD integral breadth acquired in a Siemens D5000 diffractometer using $\text{Cu K}\alpha$ radiation. Following the Williamson-Hall method⁷⁴, ϵ was obtained following the equation:

$$\beta^2 \cos^2(\theta) = \frac{\lambda_{a1}}{L_{\perp}} + 16\epsilon^2 \sin^2(\theta),$$

where β and θ are respectively the integrated breadth and the position of the (001) YBCO Bragg peaks after the subtraction of the contribution from the instrument. λ_{a1} is the wavelength of the $\text{Cu K}\alpha_1$ radiation and L_{\perp} is the coherent volume size perpendicular to the scattering vector. The scanning transmission electron microscopy observations were performed using an FEI Titan 60–300 kV microscope operated in STEM mode at 300 kV, which is equipped with an X-FEG gun, a CESCOR Cs-probe corrector, a Gatan energy filter TRIDIEM 866 ERS and a monochromator.

Data availability

The data that support the findings of this study are available from the corresponding authors on reasonable request.

Received: 14 December 2021; Accepted: 20 June 2022;

Published online: 08 July 2022

References

- Paranthaman, M. P. & Izumi, T. High-performance YBCO-coated superconductor wires. *MRS Bull.* **29**, 533–541 (2004).
- Larbalestier, D., Gurevich, A., Feldmann, D. M. & Polyanski, A. High- T_c superconducting materials for electric power applications. *Nature* **414**, 368–377 (2001).
- Shiohara, Y., Yoshizumi, M., Takagi, Y. & Izumi, T. Future prospects of high T_c superconductors-coated conductors and their applications. *Phys. C Supercond.* **484**, 1–5 (2013).
- Selvamanickam, V. et al. Enhanced critical currents in (Gd,Y)Ba₂Cu₃O_xBa superconducting tapes with high levels of Zr addition. *Supercond. Sci. Technol.* **26**, 035006 (2013).
- Obradors, X. & Puig, T. Coated conductors for power applications: materials challenges. *Supercond. Sci. Technol.* **27**, 044003 (2014).
- MacManus-Driscoll, J. L. & Wimbush, S. C. Processing and application of high-temperature superconducting coated conductors. *Nat. Rev. Mater.* **6**, 587–604 (2021).
- Malozemoff, A. P. Second-generation high-temperature superconductor wires for the electric power grid. *Annu. Rev. Mater. Res.* **42**, 373–397 (2012).
- Weijers, H. W. et al. High field magnets with HTS conductors. *IEEE Trans. Appl. Supercond.* **20**, 576–582 (2010).
- Weijers, H. W. et al. Progress in the development and construction of a 32-T superconducting magnet. *IEEE Trans. Appl. Supercond.* **26**, 1–7 (2016).
- Iwasa, Y. & Hahn, S. First-cut design of an all-superconducting 100-T direct current magnet. *Appl. Phys. Lett.* **103**, 253507 (2013).
- Liu, J. et al. World record 32.35 tesla direct-current magnetic field generated with an all-superconducting magnet. *Supercond. Sci. Technol.* **33**, 03LT01 (2020).
- Trociewitz, U. P. et al. 35.4 T field generated using a layer-wound superconducting coil made of (RE)Ba₂Cu₃O_{7-x} (RE = rare earth) coated conductor. *Appl. Phys. Lett.* **99**, 202506 (2011).
- Song, J. B. et al. Review of core technologies for development of 2G HTS NMR/MRI magnet: a status report of progress in Korea University. *Results Phys.* **7**, 3264–3276 (2017).
- Creely, A. J. et al. Overview of the SPARC tokamak. *J. Plasma Phys.* **86**, 865860502 (2020).
- Greenwald, M. Status of the SPARC physics basis. *J. Plasma Phys.* **86**, 861860501 (2020).
- Molodyk, A. et al. Development and large volume production of extremely high current density YBa₂Cu₃O₇ superconducting wires for fusion. *Sci. Rep.* **11**, 2084 (2021).
- Rossi, L. & Senatore, C. HTS accelerator magnet and conductor development in Europe. *Instruments* **5**, 8 (2021).
- Haran, K. S. et al. High power density superconducting rotating machines—development status and technology roadmap. *Supercond. Sci. Technol.* **30**, 123002 (2017).
- Shikimachi, K. et al. System coordination of 2 GJ class YBCO SMES for power system control. *IEEE Trans. Appl. Supercond.* **19**, 2012–2018 (2009).
- Zimmermann, A. W. & Sharkh, S. M. Design of a 1 MJ/100 kW high temperature superconducting magnet for energy storage. *Energy Rep.* **6**, 180–188 (2020).
- Radebaugh, R. Cryocoolers: the state of the art and recent developments. *J. Phys. Condens. Matter* **21**, 164219 (2009).
- Fisher, D. S., Fisher, M. P. A. & Huse, D. A. Thermal fluctuations, quenched disorder, phase transitions, and transport in type-II superconductors. *Phys. Rev. B* **43**, 130–159 (1991).
- Dekker, C., Eidelloth, W. & Koch, R. H. Measurement of the exponent μ in the low-temperature phase of YBa₂Cu₃O_{7-x} films in a magnetic field: direct evidence for a Vortex-Glass phase. *Phys. Rev. Lett.* **68**, 3347–3350 (1992).
- Nelson, D. R. & Vinokur, V. M. Boson localization and correlated pinning of superconducting vortex arrays. *Phys. Rev. B* **48**, 13060–13097 (1993).
- Jiang, W. et al. Evidence of a Bose-glass transition in superconducting YBa₂Cu₃O₇ single crystals with columnar defects. *Phys. Rev. Lett.* **72**, 550–553 (1994).
- Civale, L. et al. Vortex confinement by columnar defects in YBa₂Cu₃O₇ crystals: enhanced pinning at high fields and temperatures. *Phys. Rev. Lett.* **67**, 648–651 (1991).
- Foltyn, S. R. et al. Materials science challenges for high-temperature superconducting wire. *Nat. Mater.* **6**, 631–642 (2007).
- Puig, T. et al. Vortex pinning in chemical solution nanostructured YBCO films. *Supercond. Sci. Technol.* **21**, 034008 (2008).
- Matsumoto, K. & Mele, P. Artificial pinning center technology to enhance vortex pinning in YBCO coated conductors. *Supercond. Sci. Technol.* **23**, 014001 (2010).
- Obradors, X. et al. Nanostructured Superconductors with Efficient Vortex Pinning. *Comprehensive Nanoscience and Technology* Vol. 3 (eds Andrews, D. L. et al.) 303–349 (Amsterdam: Elsevier, 2011).
- Kwok, W.-K. et al. Vortices in high-performance high-temperature superconductors. *Rep. Prog. Phys.* **79**, 116501 (2016).
- Majkic, G. et al. Engineering current density over 5 kAmm⁻² at 4.2 K, 14 T in thick film REBCO tapes. *Supercond. Sci. Technol.* **31**, 10LT01 (2018).
- Haugan, T., Barnes, P. N., Wheeler, R., Meisenkothen, F. & Sumption, M. Addition of nanoparticle dispersions to enhance flux pinning of the YBa₂Cu₃O_{7-x} superconductor. *Nature* **430**, 867–870 (2004).
- Wang, H. et al. Microstructure and transport properties of Y-rich YBa₂Cu₃O_{7-δ} thin films. *J. Appl. Phys.* **100**, 053904 (2006).
- Llordés, A. et al. Nanoscale strain-induced pair suppression as a vortex-pinning mechanism in high-temperature superconductors. *Nat. Mater.* **11**, 329–336 (2012).
- Miura, M. et al. Tuning nanoparticle size for enhanced functionality in perovskite thin films deposited by metal organic deposition. *NPG Asia Mater.* **9**, e447 (2017).
- Haberhorn, N., Kim, J., Suárez, S., Lee, J.-H. & Moon, S. H. Influence of random point defects introduced by proton irradiation on the flux creep rates and magnetic field dependence of the critical current density J_c of co-evaporated GdBa₂Cu₃O_{7-δ} coated conductors. *Supercond. Sci. Technol.* **28**, 125007 (2015).
- Gazquez, J. et al. Emerging diluted ferromagnetism in high- T_c superconductors driven by point defect clusters. *Adv. Sci.* **3**, 1500295 (2016).
- Goyal, A. et al. Irradiation-free, columnar defects comprised of self-assembled nanodots and nanorods resulting in strongly enhanced flux-pinning in YBa₂Cu₃O_{7-δ} films. *Supercond. Sci. Technol.* **18**, 1533 (2005).
- Opherden, L. et al. Large pinning forces and matching effects in YBa₂Cu₃O_{7-δ} thin films with Ba₂Y(Nb/Ta)O₆ nano-precipitates. *Sci. Rep.* **6**, 21188 (2016).
- Palau, A. et al. Crossover between channeling and pinning at twin boundaries in YBa₂Cu₃O₇ thin films. *Phys. Rev. Lett.* **97**, 257002 (2006).
- Rouco, V. et al. Role of twin boundaries on vortex pinning of CSD YBCO nanocomposites. *Supercond. Sci. Technol.* **27**, 125009 (2014).
- Dam, B. et al. Origin of high critical currents in YBa₂Cu₃O_{7-δ} superconducting thin films. *Nature* **399**, 439–442 (1999).
- MacManus-Driscoll, J. L. et al. Strongly enhanced current densities in superconducting coated conductors of YBa₂Cu₃O_{7-x} + BaZrO₃. *Nat. Mater.* **3**, 439–443 (2004).
- Maivorov, B. et al. Synergetic combination of different types of defect to optimize pinning landscape using BaZrO₃-doped YBa₂Cu₃O₇. *Nat. Mater.* **8**, 398–404 (2009).
- Matsumoto, K. et al. Irreversibility fields and critical current densities in strongly pinned YBa₂Cu₃O_{7-x} films with artificial pinning centers. *IEEE Trans. Appl. Supercond.* **25**, 1–6 (2015).
- Sieger, M. et al. BaHfO₃-doped thick YBa₂Cu₃O_{7-δ} films on highly alloyed textured Ni-W tapes. *IEEE Trans. Appl. Supercond.* **25**, 1–4 (2015).
- Majkic, G., Pratap, R., Xu, A., Galstyan, E. & Selvamanickam, V. Over 15 MA/cm² of critical current density in 4.8 μm thick, Zr-doped (Gd,Y)Ba₂Cu₃O_x superconductor at 30 K, 3T. *Sci. Rep.* **8**, 6982 (2018).
- Usoskin, A. et al. Double-disordered HTS-coated conductors and their assemblies aimed for ultra-high fields: large area tapes. *IEEE Trans. Appl. Supercond.* **28**, 1–6 (2018).
- Kihlstrom, K. J. et al. Large enhancement of the in-field critical current density of YBCO coated conductors due to composite pinning landscape. *Supercond. Sci. Technol.* **34**, 015011 (2021).
- Tsuchiya, Y. et al. Flux pinning landscape up to 25T in SmBa₂Cu₃O_y films with BaHfO₃ nanorods fabricated by low-temperature growth technique. *Supercond. Sci. Technol.* **30**, 104004 (2017).
- Feighan, J. P. F., Kursumovic, A. & MacManus-Driscoll, J. L. Materials design for artificial pinning centres in superconductor PLD coated conductors. *Supercond. Sci. Technol.* **30**, 123001 (2017).
- Xu, A. et al. Strongly enhanced vortex pinning from 4 to 77 K in magnetic fields up to 31 T in 15 mol.% Zr-added (Gd, Y)-Ba-Cu-O superconducting tapes. *APL Mater.* **2**, 046111 (2014).
- Gutiérrez, J. et al. Strong isotropic flux pinning in solution-derived YBa₂Cu₃O_{7-x} nanocomposite superconductor films. *Nat. Mater.* **6**, 367–373 (2007).
- Cayado, P. et al. Epitaxial YBa₂Cu₃O_{7-x} nanocomposite thin films from colloidal solutions. *Supercond. Sci. Technol.* **28**, 124007 (2015).
- Li, Z. et al. Control of nanostructure and pinning properties in solution deposited YBa₂Cu₃O_{7-x} nanocomposites with preformed perovskite nanoparticles. *Sci. Rep.* **9**, 5828 (2019).
- Stangl, A., Palau, A., Deutscher, G., Obradors, X. & Puig, T. Ultra-high critical current densities of superconducting YBa₂Cu₃O_{7-δ} thin films in the overdoped state. *Sci. Rep.* **11**, 8176 (2021).
- Palau, A. et al. Disentangling vortex pinning landscape in chemical solution deposited superconducting YBa₂Cu₃O_{7-x} films and nanocomposites. *Supercond. Sci. Technol.* **31**, 034004 (2018).

59. Bartolomé, E. et al. Embedded magnetism in $\text{YBa}_2\text{Cu}_3\text{O}_7$ associated with Cu–O vacancies within nanoscale intergrowths: implications for superconducting current performance. *ACS Appl. Nano Mater.* **3**, 3050–3059 (2020).
60. Guzman, R. et al. Probing localized strain in solution-derived $\text{YBa}_2\text{Cu}_3\text{O}_{7-\delta}$ nanocomposite thin films. *Phys. Rev. Mater.* **1**, 024801 (2017).
61. Gazquez, J. et al. Structural defects in trifluoroacetate derived $\text{YBa}_2\text{Cu}_3\text{O}_7$ thin films. *Supercond. Sci. Technol.* **25**, 065009 (2012).
62. Guzman, R. et al. Strain-driven broken twin boundary coherence in $\text{YBa}_2\text{Cu}_3\text{O}_{7-\delta}$ nanocomposite thin films. *Appl. Phys. Lett.* **102**, 081906 (2013).
63. Tachiki, M. & Takahashi, S. Intrinsic pinning in cuprate superconductors. *Appl. Supercond.* **2**, 305–313 (1994).
64. Civale, L. et al. Identification of intrinsic ab-plane pinning in $\text{YBa}_2\text{Cu}_3\text{O}_7$ thin films and coated conductors. *IEEE Trans. Applied Supercond.* **15**, 2808–2811 (2005).
65. Vallès, F. et al. Angular flux creep contributions in $\text{YBa}_2\text{Cu}_3\text{O}_{7-\delta}$ nanocomposites from electrical transport measurements. *Sci. Rep.* **8**, 5924 (2018).
66. Blatter, G., Feigel'man, M. V., Geshkenbein, V. B., Larkin, A. I. & Vinokur, V. M. Vortices in high-temperature superconductors. *Rev. Mod. Phys.* **66**, 1125–1388 (1994).
67. Plain, J., Puig, T., Sandiumenge, F., Obradors, X. & Rabier, J. Microstructural influence on critical currents and irreversibility line in melt-textured $\text{YBa}_2\text{Cu}_3\text{O}_{7-x}$ reannealed at high oxygen pressure. *Phys. Rev. B* **65**, 104526 (2002).
68. Polat, O. et al. Thickness dependence of magnetic relaxation and E–J characteristics in superconducting (Gd–Y)–Ba–Cu–O films with strong vortex pinning. *Phys. Rev. B* **84**, 024519 (2011).
69. Xu, A., Braccini, V., Jaroszynski, J., Xin, Y. & Larbaestier, D. C. Role of weak uncorrelated pinning introduced by BaZrO_3 nanorods at low-temperature in $(\text{Y,Gd})\text{Ba}_2\text{Cu}_3\text{O}_x$ thin films. *Phys. Rev. B* **86**, 115416 (2012).
70. Krusin-Elbaum, L. et al. Bose-glass melting in YBaCuO crystals with correlated disorder. *Phys. Rev. Lett.* **72**, 1914–1917 (1994).
71. Braccini, V. et al. Properties of recent IBAD–MOCVD coated conductors relevant to their high field, low temperature magnet use. *Supercond. Sci. Technol.* **24**, 035001 (2011).
72. Mezzetti, E. et al. Control of the critical current density in $\text{YBa}_2\text{Cu}_3\text{O}_{7-\delta}$ films by means of intergrain and intragrain correlated defects. *Phys. Rev. B* **60**, 7623–7630 (1999).
73. Blatter, G., Geshkenbein, V. B. & Larkin, A. I. From isotropic to anisotropic superconductors: a scaling approach. *Phys. Rev. Lett.* **68**, 875–878 (1992).
74. Williamson, G. K. & Hall, W. H. X-ray line broadening from filed aluminium and wolfram. *Acta Metall.* **1**, 22–31 (1953).
75. Civale, L. et al. Angular-dependent vortex pinning mechanisms in $\text{YBa}_2\text{Cu}_3\text{O}_7$ coated conductors and thin films. *Appl. Phys. Lett.* **84**, 2121–2123 (2004).
76. Soler, L. et al. Ultrafast transient liquid assisted growth of high current density superconducting films. *Nat. Commun.* **11**, 344 (2020).
77. Villarejo, B. et al. Pyrolysis study of solution-derived superconducting $\text{YBa}_2\text{Cu}_3\text{O}_7$ films: disentangling the physico-chemical transformations. *J. Mater. Chem. C* **8**, 10266–10282 (2020).
78. Kogan, V. G. & Zhelezina, N. V. Field dependence of the vortex core size. *Phys. Rev. B* **71**, 134505 (2005).
79. Sonier, J. E. Muon spin rotation studies of electronic excitations and magnetism in the vortex cores of superconductors. *Rep. Prog. Phys.* **70**, 1717–1755 (2007).
80. Rouco, V. et al. Vortex creep in TFA–YBCO nanocomposite films. *Supercond. Sci. Technol.* **27**, 115008 (2014).
81. Roma, N. et al. Acid anhydrides: a simple route to highly pure organometallic solutions for superconducting films. *Supercond. Sci. Technol.* **19**, 521–527 (2006).
82. Llordés, A. et al. Evolution of metal-trifluoroacetate precursors in the thermal decomposition toward high-performance $\text{YBa}_2\text{Cu}_3\text{O}_7$ superconducting films. *Chem. Mater.* **22**, 1686–1694 (2010).
83. Obradors, X. et al. Growth, nanostructure and vortex pinning in superconducting $\text{YBa}_2\text{Cu}_3\text{O}_7$ thin films based on trifluoroacetate solutions. *Supercond. Sci. Technol.* **25**, 123001 (2012).
84. Pop, C. et al. Growth of all-chemical high critical current $\text{YBa}_2\text{Cu}_3\text{O}_{7-\delta}$ thick films and coated conductors. *Supercond. Sci. Technol.* **32**, 015004 (2019).
85. Villarejo, B. et al. High performance of superconducting $\text{YBa}_2\text{Cu}_3\text{O}_7$ thick films prepared by single-deposition inkjet printing. *ACS Appl. Electron. Mater.* **3**, 3948–3961 (2021).
86. Li, Z. et al. Accelerated growth by flash heating of high critical current trifluoroacetate solution derived epitaxial superconducting $\text{YBa}_2\text{Cu}_3\text{O}_7$ films. *J. Mater. Chem. C* **7**, 4748–4759 (2019).
87. Chamorro, N. et al. Hybrid approach to obtain high-quality BaMO_3 perovskite nanocrystals. *RSC Adv.* **10**, 28872–28878 (2020).
88. De Keukeleere, K. et al. Superconducting $\text{YBa}_2\text{Cu}_3\text{O}_{7-\delta}$ nanocomposites using preformed ZrO_2 nanocrystals: growth mechanisms and vortex pinning properties. *Adv. Electron. Mater.* **2**, 1600161 (2016).

Acknowledgements

The authors acknowledge financial support from Spanish Ministry of Economy and Competitiveness through the “Severo Ochoa” Programme for Centres of Excellence in R&D (Grant No. SEV-2015-0496), ULTRASUPERTAPE (ERC-2014-ADG-669504), EUROTAPES project (FP7-NMP-Large-2011-280432), the CONSOLIDER Excellence Network (Grant No. MAT2015-68994-REDC), COACHSUPENERGY project (Grant No. MAT2014-56063-C2-1-R and SuMaTe RTI2018-095853-B-C21, co-financed by the European Regional Development Fund), and from the Catalan Government with Grant No. 2014-SGR-753 and 2017-SGR-1519. Authors also thank the network collaboration of EU COST action NANOCOHYBRI CA16218. We also acknowledge the Scientific Services at ICMAB and Z. Li and P. Cayado for the growth of the studied samples. A portion of this work was performed at the National High Magnetic Field Laboratory, which is supported by the National Science Foundation Cooperative Agreement No. DMR-1644779 and the State of Florida.

Author contributions

F.V., A.P. and T.P. designed the experimental study. F.V. performed the main experimental work and analysed the data. D.A., A-M.C., J.J. and F.V. prepared the experimental setup and performed the measurements at very high magnetic fields. B.M. performed and analysed the STEM observations. F.V. and T.P. prepared the manuscript with contributions from co-authors. X.O., D.L., T.P., A.P., B.M., J.J., A-M.C., D.A. and F.V. contributed to the scientific discussion.

Competing interests

The authors declare no competing interests.

Additional information

Supplementary information The online version contains supplementary material available at <https://doi.org/10.1038/s43246-022-00266-y>.

Correspondence and requests for materials should be addressed to Ferran Vallès or Teresa Puig.

Peer review information *Communications Materials* thanks the anonymous reviewers for their contribution to the peer review of this work. Primary Handling Editors: Nicola Poccia and Aldo Isidori. Peer reviewer reports are available.

Reprints and permission information is available at <http://www.nature.com/reprints>

Publisher's note Springer Nature remains neutral with regard to jurisdictional claims in published maps and institutional affiliations.



Open Access This article is licensed under a Creative Commons Attribution 4.0 International License, which permits use, sharing, adaptation, distribution and reproduction in any medium or format, as long as you give appropriate credit to the original author(s) and the source, provide a link to the Creative Commons license, and indicate if changes were made. The images or other third party material in this article are included in the article's Creative Commons license, unless indicated otherwise in a credit line to the material. If material is not included in the article's Creative Commons license and your intended use is not permitted by statutory regulation or exceeds the permitted use, you will need to obtain permission directly from the copyright holder. To view a copy of this license, visit <http://creativecommons.org/licenses/by/4.0/>.

© The Author(s) 2022